JCTC Journal of Chemical Theory and Computation

pubs.acs.org/JCTC Article

Holographic Gaussian Boson Sampling with Matrix Product States on 3D cQED Processors

Ningyi Lyu, Paul Bergold, Micheline B. Soley, Chen Wang, and Victor S. Batista*

Cite This: J. Chem. Theory Comput. 2024, 20, 6402−6413 Read Online

ACCESS | Metrics & More | Article Recommendations | Supporting Information

ABSTRACT: We introduce quantum circuits for simulations of multimode state vectors on 3D circuit quantum electrodynamics (cQED) processors using matrix product state representations. The circuits are demonstrated as applied to simulations of molecular docking based on holographic Gaussian boson sampling (GBS), as illustrated for the binding of a thiol-containing aryl sulfonamide ligand to the tumor necrosis factor-α converting enzyme receptor. We show that cQED devices with a modest number of modes could be employed to simulate multimode systems by repurposing working modes through measurement and reinitialization. We anticipate that a wide range of GBS applications could be implemented on compact 3D cQED processors analogously using the holographic approach. Simulations on qubit-based quantum computers could be implemented analogously using circuits that represent continuous variables in terms of truncated expansions of Fock states.

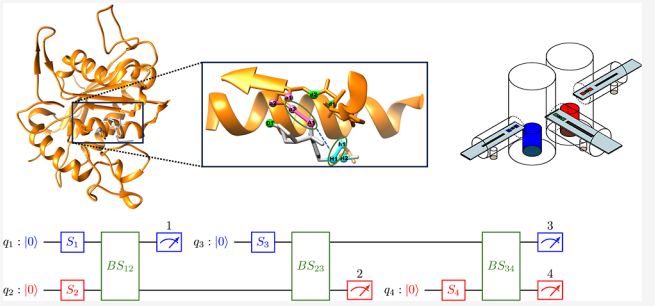

1. INTRODUCTION

Graph theory plays a crucial role in computational chemistry, aiding in the modeling of molecules, chemical data sets, and reaction networks, as shown in recent studies.[1−5] It enables easier calculations in diverse areas from cheminformatics[6] to quantum chemistry,[7,8] and polymer chemistry.[9] Despite its utility, the complex nature of molecules and chemical databases often results in large graphs, challenging the capabilities of classical algorithms. For instance, several classes of problems require the computation of permanents, which is known to be #P-hard, escalating to #P-complete for binary matrices.[10] Such complexity places these computations beyond the reach of conventional methods.[11] Near-term quantum computers that implement boson sampling (BS)[12] offer a promising quantum solution. Here, we explore the application of BS to simulations of molecular docking, focusing on the possibility of sampling subgraphs describing the interactions between a molecule and a biological receptor using compact bosonic processors.

BS in its fundamental form involves the sampling of photons dispersed through a passive N-mode linear interferometer, as proposed by Aaronson and Arkhipov,[12] building upon the work by Troyansky and Tishby on quantum calculations of permanents and determinants.[13] In such experiments, the outcome distribution is determined by the permanent of the $N \times N$ matrix representing the transition probability amplitudes of the linear interferometer. As a result, BS enables the sampling of bosons from a distribution that would be challenging to simulate classically for large values of N, offering a promising approach to tackling problems previously considered intractable.

BS has been implemented on a diverse array of hardware platforms,[14−17] offering versatility and potential in applications of chemical relevance.[18−22] Notably, BS has been applied to compute the vibronic spectra of triatomic molecules using 3D circuit quantum electrodynamics (cQED) processors[18,19] and to simulate molecular docking on photonic devices.[20−22] In fact, the initial BS sampling setup utilized optical photons. However, the efficient generation and detection of nonclassical light states pose significant challenges.[18,20] Here, we explore the use of microwave photons within the cQED architecture,[23] offering a promising alternative technology with unique advantages for implementing BS.

The cQED architecture stands at the forefront of quantum technology, featuring superconducting qubits based on Josephson junctions that are strongly coupled to the modes of superconducting microwave cavities. This setup facilitates efficient information exchange and enables universal quantum control over quantum states. Moreover, it supports quantum nondemolition measurements of photon numbers within the microwave cavities of the superconducting circuits. The

Received: March 25, 2024
Revised: June 10, 2024
Accepted: June 10, 2024
Published: July 5, 2024

https://doi.org/10.1021/acs.jctc.4c00384
J. Chem. Theory Comput. 2024, 20, 6402−6413

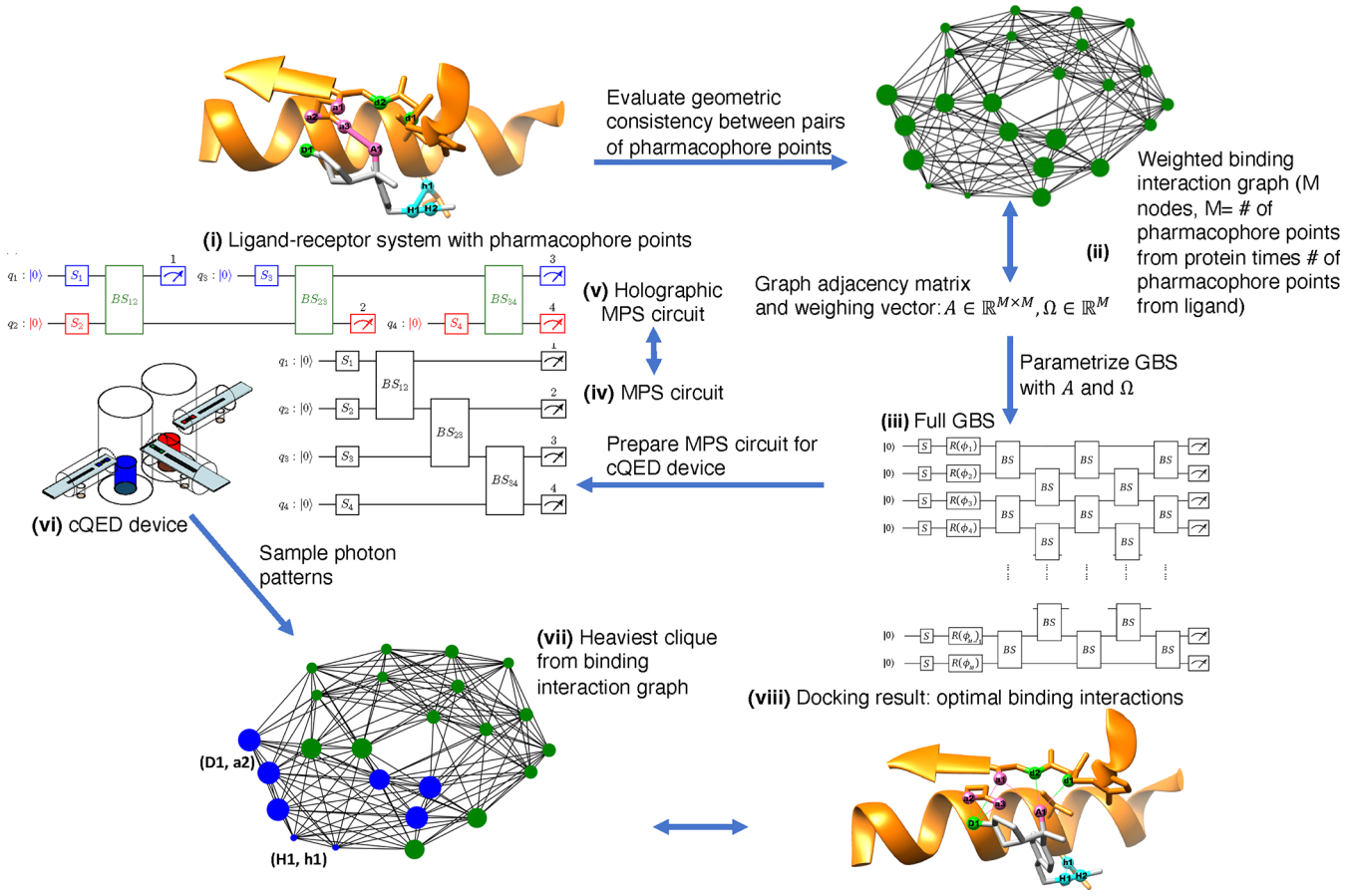

Figure 1. Schematic representation of the GBS approach implemented to investigate molecular docking due to a ligand−receptor interaction (i). The interactions are represented by a graph where vertices correspond to pairs of interactions between pharmacophores in the ligand and in the receptor, while the edges connect pairs of contact that can be established simultaneously (ii). The graph adjacency matrix is used to define the covariance matrix of a multimode Gaussian state, generated by a passive linear interferometer of beam splitters (iii). Sampling bosons from that distribution reveals the subsets of compatible pairs of interactions that can be established simultaneously. To sample from that distribution, initially a MPS representation of the circuit is generated (iv), which can be implemented with a holographic approach (v) on a compact cQED device (vi). The observed photon patterns in the output modes indicate the heavier cliques (vii), from which optimal ligand−receptor interactions are established.

precision in photon counting afforded by this architecture enhances the feasibility of implementing BS as evidenced by previous studies.[18]

In this paper, we explore the possibility of implementing BS simulations of molecular docking using 3D cQED processors. Molecular docking, an essential computational technique for drug design, predicts the binding configuration and most favorable interactions of a molecule and its receptor. This task is difficult for classical computers due to the need to perform an exhaustive search of possible molecular configurations. BS, with its ability to sample from a distribution defined by the permanent of the interaction matrix, holds promise for significantly enhancing the efficiency of molecular docking simulations, offering a novel approach to overcoming the limitations of traditional computational methods.

In this study, we focus on Gaussian boson sampling (GBS), a version of BS based on multimode Gaussian states.[24−26] We explore the possibility of simulating GBS using 3D cQED processors employing a holographic approach.[14,27,28] This method is inspired by the successful utilization of GBS in conjunction with 3D cQED processors for simulations of molecules.[18]

Our methodology begins by approximating the multimode state vectors as low-rank matrix product states[29,30] (MPS, also called tensor trains[31−33]), followed by the variational parametrization of quantum circuits to represent these state vectors. The resulting circuits are executed holographically by repurposing modes,[14,27,28] with the term "holographic" reflecting the dimension reduction benefit from the repurposing algorithm, in echo with holography that constructs 3D image from 2D snapshots. This allows for hardware efficiency, enabling simulations of a few tens of modes with as few as 2−3 microwave modes in the cQED devices.

Our numerical simulations reveal that these cQED circuits could accurately simulate multimode Gaussian states, closely matching the benchmark Gaussian states of conventional GBS applied to molecular docking problems. Therefore, we anticipate that these findings will pave the way for experimental investigations of compact 3D cQED devices into molecular docking and other subgraph isomorphism problems,[34] highlighting the potential for conducting realistic simulations with numerous modes on modestly sized cQED devices.

https://doi.org/10.1021/acs.jctc.4c00384
J. Chem. Theory Comput. 2024, 20, 6402−6413

2. METHODOLOGY

2.1. Molecular Docking by GBS. Figure 1 shows a schematic representation of the GBS methodology implemented to investigate molecular docking. Ligand−receptor interactions (Figure 1i) are established by ligand and receptor pharmacophores, as described in Section 2.2. The interaction graph (Figure 1ii) describes the network of compatible pairs of interactions where the vertices correspond to pairs of interactions while the edges connect interactions that can be established simultaneously. Section 2.3 outlines how the interaction graph is mapped into a GBS device to generate a multimode Gaussian state vector, with the covariance parametrized by the adjacency matrix of the interaction graph (Figure 1iii).

Our simulations represent the state vector in MPS format (Figure 1iv), allowing for a holographic implementation (Figure 1v) using a cQED device (Figure 1vi). Sampling from that state vector distribution reveals subgraphs with maximum cliques (Figure 1vii) corresponding to subsets of interactions that can be established simultaneously (Figure 1viii). Section 2.4 outlines experimental strategies for holographic implementations of GBS based on MPS networks with one and two layers of two-mode beam splitters, parametrized to approximate the full GBS network. Section 2.5 describes cQED devices based on bosonic 3D cQED devices for simulations of holographic MPS networks.

2.2. Interaction Graph. Molecular docking algorithms predict favorable binding configurations of ligands (or drug-like molecules) as determined by interactions established by pharmacophores in the ligand with complementary pharmacophores in the target macromolecule (receptor). Configurations are ranked in terms of docking scores that give a rough estimate of relative binding affinities based on molecular descriptors.

Reliable determination of docking scores for a series of ligands and favorable binding configurations is particularly valuable since it allows for rapid in silico screening of a large number of compounds. That process can quickly identify promising lead compounds for subsequent more accurate analysis and discard unsuitable ligands. In the simplest approach, both the ligand and the receptor are approximated as rigid bodies, although methods that account for the inherent flexibility of the ligand and the receptor are available.[35] Favorable ligand orientations at the binding site can be revealed by using the isomorphous subgraph matching method, as implemented in the DOCK 4.0, FLOG, and SQ algorithms.[34,36−39] In that formulation of the binding problem, the ligand−receptor interactions are represented by the so-called interaction graph $G(V, E)$, shown in Figure 2. Here, the vertices V represent ligand−receptor interactions established by pharmacophores,[40] while the edges E link pairs of interactions that can occur concurrently since the drug pharmacophores involved in these interactions are at the same distance apart as the corresponding pharmacophores in the receptor.

The interaction graph $G(V, E)$ is defined by its $M \times M$ adjacency matrix A, where $M > 1$ is the total number of possible ligand−receptor interactions, with $A_{ij} = 1$ if the interactions i and j are compatible (if both interactions can be established simultaneously) and $A_{ij} = 0$ otherwise. To model the interaction strength between pharmacophores, we weight every vertex according the type of pharmacophores i and j, biasing the strength of the intermolecular interactions with a preparameterized potential.[41−43] Having defined the adjacency, the problem of docking is reduced to the so-called maximum clique problem,[34] which involves finding the largest fully connected subgraph within the graph, representing the largest set of compatible interactions as determined by the types of pharmacophore interactions and the interpharmacophore distances.

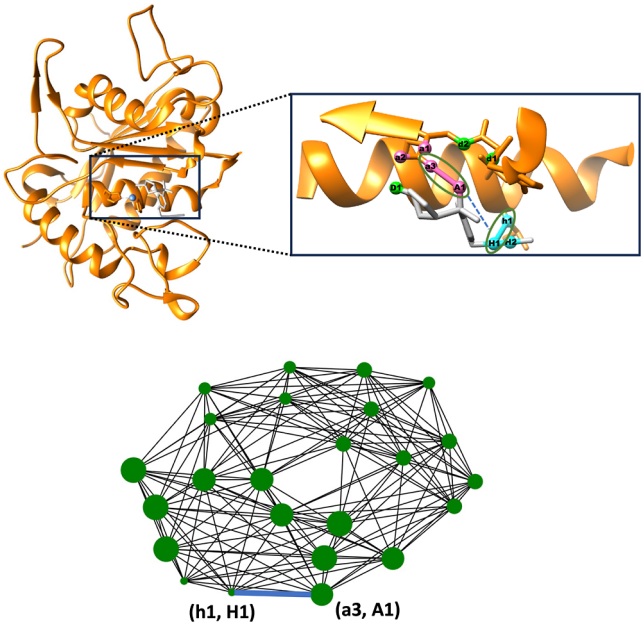

Figure 2. (Top left) Crystal structure of the tumor necrosis factor-α converting enzyme receptor (TACE, orange) with thiol-containing aryl sulfonamide ligand (AS, gray). (Top right) Zoomed-in binding site with four pharmacophores in the ligand (A1, D1, H1, and H2) and six in the receptor (a1, a2, a3, d1, d2, and h1). Two pairs of binding interactions (a3, A1) and (h1, H1) can be concurrently established, as shown by blue dashed lines. (Bottom) Binding interaction graph of all possible pairwise ligand−receptor interactions. Larger nodes indicate heavier weights (stronger interactions).

2.3. Maximum Clique Subgraph. GBS addresses the maximum clique problem, as shown below, through preparation of a multimode Gaussian state vector whose covariance matrix is parametrized by the adjacency matrix of the ligand−receptor interaction graph. The state vector is generated from a vacuum state using single-mode squeezing and a multimode linear interferometer. For simplicity, it is assumed that the mode count significantly exceeds the average photon number, resulting in either a single photon or no photon detection ($n_j \in \{0, 1\}$) in each mode j.

2.3.1. Multimode Gaussian of Bosonic Modes. A Gaussian state of a system with M bosonic modes, designated as j, with creation and annihilation operators $\hat{a}_j^\dagger$ and $\hat{a}_j$, can be described by the density matrix

$$\hat{\rho} = (2\pi)^{-M}|\det(\sigma)|^{-1/2} e^{-1/2(\hat{\xi}-d)^\dagger \sigma^{-1}(\hat{\xi}-d)} \quad (1)$$

where $\hat{\xi} = (\hat{a}_1, ..., \hat{a}_M, \hat{a}_1^\dagger, ..., \hat{a}_M^\dagger)^T$ is a $2M$-component vector of operators. According to eq 1, the Gaussian state is defined completely by its first and second statistical moments, d and σ, respectively. The first moments

$$d_j = \mathrm{Tr}[\hat{\rho}\,\hat{\xi}_j] \quad (2)$$

https://doi.org/10.1021/acs.jctc.4c00384
J. Chem. Theory Comput. 2024, 20, 6402−6413

describe the mode displacements, while the second moments

$$\sigma_{ij} = \frac{1}{2}\mathrm{Tr}[\hat{\rho}\{(\hat{\xi}_i - d_i), (\hat{\xi}_j - d_j)^\dagger\}] \tag{3}$$

define the $2M \times 2M$ covariance matrix σ in terms of the anticommutators

$$\{(\hat{\xi}_i - d_i), (\hat{\xi}_j - d_j)^\dagger\} = (\hat{\xi}_i - d_i)(\hat{\xi}_j - d_j)^\dagger + (\hat{\xi}_j - d_j)^\dagger(\hat{\xi}_i - d_i) \tag{4}$$

Measurements of the modes, when the system is described by the Gaussian statevector defined by eq 1, report whether a photon is detected or not in each mode, as follows: $\overline{n} = (n_1, n_2, ..., n_M)^T$, where $n_j \in \{0, 1\}$ with $j = 1, ..., M$. In the realm of molecular docking, each mode j symbolizes a distinct interaction between a pharmacophore of the drug and a pharmacophore of the receptor. Detecting a photon in a particular mode suggests that the corresponding interaction is established, whereas the absence of photons signifies a disruption of that interaction.

2.3.2. Probability Distribution. The probability distribution of outputs $\overline{n}$, obtained by measuring the multimode Gaussian in the Fock basis, is defined, as follows

$$\Pr(\overline{n}) = \mathrm{Tr}[\hat{\rho}\hat{\overline{n}}] \tag{5}$$

where $\hat{\overline{n}} = \bigotimes_{j=1}^{M} \hat{n}_j$ is the tensor product of number state operators $\hat{n}_j = |n_j\rangle\langle n_j|$ corresponding to the probability of observing n_j bosons in output mode j. The right-hand side of eq 5 can be expanded by using the P-representation of operators, as follows (Supporting Information 1)

$$\mathrm{Tr}\left[\bigotimes_{j=1}^{M} |n_j\rangle\langle n_j|\hat{\rho}\right] = \int P_{\bigotimes_{j=1}^{M} |n_j\rangle\langle n_j|}(\alpha) Q(\alpha)\, \mathrm{d}^2\alpha, \tag{6}$$

where

$$P_{\bigotimes_{j=1}^{M} |n_j\rangle\langle n_j|}(\alpha) = \prod_{j=1}^{M} \frac{e^{|\alpha_j|^2}}{n_j!} \frac{\partial^{2n_j}}{\partial^{n_j}\alpha_j \partial^{n_j}\alpha_j^*} \delta^2\alpha_j \tag{7}$$

$Q(\alpha)$, introduced by eq 6, is the Husimi function of the Gaussian state, defined as follows (Supporting Information 1)

$$Q(\alpha) = \pi^{-M}\langle\alpha|\hat{\rho}|\alpha\rangle = \frac{\pi^{-M}}{\sqrt{|\det(\sigma_Q)|}} e^{-\alpha^\dagger \sigma_Q^{-1}\alpha} \tag{8}$$

where $\alpha = (\alpha_1, ..., \alpha_M, \alpha_1^*, ..., \alpha_M^*)^T$ and $\sigma_Q = \sigma + I_{2M}/2$, with I_{2M} being the $2M \times 2M$ identity matrix. The Husimi function obtained with eq 8, using the Gaussian density matrix introduced by eq 1, can be substituted into eq 6 to obtain (Supporting Information 2)

$$\Pr(\overline{n}) = \frac{1}{\sqrt{|\det(\sigma_Q)|}} \prod_{j=1}^{M} \frac{1}{n_j!} \frac{\partial^{2n_j}}{\partial^{n_j}\alpha_j \partial^{n_j}\alpha_j^*} e^{\frac{1}{2}\alpha^T K \alpha}\Big|_{\alpha_j = 0} \tag{9}$$

where

$$K = X_{2M}(I_{2M} - \sigma_Q^{-1}) \tag{10}$$

with $X_{2M} = \begin{bmatrix} 0 & I_M \\ I_M & 0 \end{bmatrix}$. Since $n_j \in \{0, 1\}$, the multivariate derivatives in eq 9 can be easily evaluated by using the high-order chain rule given by the Faa di Bruno's formula (Supporting Information, Section 3), as follows

$$\Pr(\overline{n}) = \frac{1}{\overline{n}!\sqrt{|\det(\sigma_Q)|}} \sum_{\rho \in P_{2N}^2} \prod_{\{i,j\} \in \rho} K_{ij} \tag{11}$$

where $N = n_1 + \cdots + n_M$ is the total number of modes, where a photon was detected according to $\overline{n}$, and $\overline{n}! = n_1!n_2!...n_M!$. Moreover, P_{2N}^2 is the set of partitions of the set $\{1, 2, ..., 2N\}$ into subsets of two indices. The summation in eq 11 is exactly the Hafnian of the $2N \times 2N$ submatrix of K with rows and columns corresponding to the modes where photons were detected (i.e., modes j with $n_j = 1$). Defining the submatrix of those modes as matrix K_S, we obtain

$$\Pr(\overline{n}) = \frac{1}{\overline{n}!\sqrt{|\det(\sigma_Q)|}} \mathrm{Haf}(K_S) \tag{12}$$

To encode graph problems into Gaussian quantum states, we consider the matrix K to be defined in terms of the graph adjacency matrix A, as follows[25]

$$K = c(A \oplus A) \tag{13}$$

where the circled plus sign denotes the construction of a block-diagonal matrix from the component matrices. Furthermore, $0 < c < \lambda_1^{-1}$ is a positive rescaling parameter, with $\lambda_1 > 0$ the maximum eigenvalue of A. Note that for an undirected graph without self-connection, A is a real symmetric matrix with all diagonal elements being 0. Since $\mathrm{Tr}[A] = 0$ implies that the eigenvalues must be either all 0 or containing both positive and negative numbers, and the only real symmetric matrix that contains all zero eigenvalues is the zero matrix, the largest eigenvalue of A must be positive for a nonzero A. In particular, the scaling factor ensures that K corresponds to a valid covariance matrix σ as in eq 10, resulting in a probability distribution $\Pr(\overline{n})$ that is bounded between zero and one. In Section 2.3.5 we show that an M-mode Gaussian state with such a K can always be prepared by a programmed optical network.

Substituting eq 13 into 12, we obtain

$$\Pr(\overline{n}) = \frac{c^N}{\overline{n}!\sqrt{|\det(\sigma_Q)|}} \mathrm{Haf}(A_S \oplus A_S) = \frac{c^N}{\overline{n}!\sqrt{|\det(\sigma_Q)|}} \mathrm{Haf}(A_S)^2 \tag{14}$$

providing the probability distribution of outputs $\overline{n}$ in terms of the Hafnian of A_S (with A_S the submatrix of A defined by the intersection of rows and columns of A corresponding to the modes where photons were detected).

2.3.3. Binary Graphs. In the simplest formulation of a binary graph, A is the $M \times M$ real and symmetric adjacency matrix with $A_{ij} \in \{0, 1\}$. $A_{ij} = 1$ denotes that nodes i and j share an edge, while $A_{ij} = 0$ denotes that nodes i and j are not connected. In the context of binding interaction graphs that are of our primary interest, a node denotes a binding interaction between a pair of pharmacophore points, connection between two nodes indicate the two binding interactions can be established simultaneously, and no connection indicates that the two binding interactions cannot be concurrently established because by establishing one interaction the other one is disrupted. This binary approach can be generalized to account for the strength of the connections using instead a weighted binding interaction graph as described later in Section 2.3.4.

https://doi.org/10.1021/acs.jctc.4c00384
J. Chem. Theory Comput. 2024, 20, 6402−6413

It is important to note that each term in the sum of the Hafnian in eq 14 represents a *perfect matching* where each node of the subgraph is connected to one (and only one) other node. As a result, the Hafnian gives the count of perfect matchings and thus reveals the number of possible ways the drug pharmacophores can concurrently establish interactions with pharmacophores in the receptor. As per eq 14, subgraphs with larger Hafnian are sampled with higher probability.

Gaussian states are prepared with covariance σ, obtained by inverting eq 10, as follows

$$\sigma = (I_{2M} - X_{2M}K)^{-1} - \frac{I_{2M}}{2} \tag{15}$$

with K defined according to eq 13. This is achieved by using a quantum circuit that integrates single-mode squeezing gates and a multimode linear interferometer, as detailed in Section 2.3.5. Sampling from the state vector generated by that circuit enables us to effectively identify the subgraphs with larger Hafnian within the interaction graph, revealing the capability of the drug to establish concurrent interactions with the receptor.

2.3.4. Weighted Graphs. Extending the method to accommodate weighted graphs beyond binary adjacency matrices A (with $A_{ij} \in \{0, 1\}$) is straightforward. This requires a weighting vector Ω, where each element $\Omega_{ii} = c(1 + w_i)$ is defined by a weight w_i assigned to the ith node. This design of the weighting vector ensures that subgraphs with a larger weight are favored during sampling.[21] In the context of molecular docking, these weights are obtained from a knowledge-based potential, where a heavier weight w_i corresponds to a stronger binding interaction.[34] For instance, if the ith node corresponds to a hydrogen bond donor−acceptor interaction, w_i would be larger than for nodes representing weaker interactions (e.g., hydrophobic contacts). The weighting vector Ω is written as a diagonal matrix $[\mathrm{diag}(\Omega) \rightarrow \Omega]$ and applied on both sides of A to generate a weighted graph adjacency matrix, as follows

$$A \rightarrow \Omega A \Omega \tag{16}$$

generates a photon distribution defined by both A and Ω, as follows

$$\begin{aligned}
\Pr(\overline{n}) &= \frac{c^N}{\overline{n}!\sqrt{|\det(\sigma_Q)|}}[\mathrm{Haf}(\Omega_S A_S \Omega_S)]^2 \\
&= \frac{c^N}{\overline{n}!\sqrt{|\det(\sigma_Q)|}}[\sum_{\rho \in P_N^2} \prod_{\{i,j\}\in\rho} \Omega_{ii} A_{ij} \Omega_{jj}]^2 \\
&= \frac{c^N}{\overline{n}!\sqrt{|\det(\sigma_Q)|}}[\det(\Omega) \sum_{\rho \in P_N^2} \prod_{\{i,j\}\in\rho} A_{ij}]^2 \\
&= \frac{c^N}{\overline{n}!\sqrt{|\det(\sigma_Q)|}}[\det(\Omega_S)\mathrm{Haf}(A_S)]^2
\end{aligned} \tag{17}$$

where Ω_S is the submatrix of Ω corresponding to the modes registering photons (the modes that also define A_S). According to eq 17, the resulting GBS with rescaled adjacency matrices has higher probability of sampling cliques with a large number of strongly interacting pharmacophores.

2.3.5. Quantum Circuit. Here, we show how to build a quantum circuit of M modes that generates the desired multimode Gaussian state with covariance defined by eq 15 with $K = c(A \oplus A)$, as necessary for GBS. In particular, we show that such a state can be obtained by passing a vacuum Gaussian state through an optical network composed of M single-mode squeezers and an M-mode interferometer, both parametrized according to A. First, we show how the single-mode squeezers and M-mode interferometer transform the M-mode vacuum state by preserving its Gaussian shape but changing its covariance. Then, we show how the squeezers and interferometer are parametrized according to A.

The single mode vacuum state $|0\rangle$ is the eigenstate of $\hat{a}$ with eigenvalue 0

$$\hat{a}|0\rangle = 0 \tag{18}$$

Therefore

$$\begin{aligned}
\langle \hat{a} \rangle_{\mathrm{vac}} &= \mathrm{Tr}[|0\rangle\langle 0|\hat{a}] = 0 \\
\langle \hat{a}^\dagger \rangle_{\mathrm{vac}} &= \mathrm{Tr}[|0\rangle\langle 0|\hat{a}^\dagger] = 0 \\
\langle \hat{a}\hat{a} \rangle_{\mathrm{vac}} &= \mathrm{Tr}[|0\rangle\langle 0|\hat{a}\hat{a}] = 0 \\
\langle \hat{a}\hat{a}^\dagger \rangle_{\mathrm{vac}} &= \mathrm{Tr}[|0\rangle\langle 0|\hat{a}\hat{a}^\dagger] = 1 \\
\langle \hat{a}^\dagger\hat{a} \rangle_{\mathrm{vac}} &= \mathrm{Tr}[|0\rangle\langle 0|\hat{a}^\dagger\hat{a}] = 0 \\
\langle \hat{a}^\dagger\hat{a}^\dagger \rangle_{\mathrm{vac}} &= \mathrm{Tr}[|0\rangle\langle 0|\hat{a}^\dagger\hat{a}^\dagger] = 0
\end{aligned} \tag{19}$$

where the subscripts indicate that the expectation values $\langle\ \rangle$ are evaluated with $\hat{\rho} = |0\rangle\langle 0|$. Substituting eq 19 into 3, we obtain the covariance matrix of the single mode vacuum state

$$\sigma_{\mathrm{vac}} = \frac{1}{2}\begin{bmatrix} 1 & 0 \\ 0 & 1 \end{bmatrix} \tag{20}$$

The single-mode squeezing operation is defined as follows

$$\hat{S}(r) = e^{(-r(\hat{a})^2 + r(\hat{a}^\dagger)^2)/2} \tag{21}$$

where $r \in \mathbb{R}$ is real-valued and is referred to as the squeezing parameter. Supporting Information 4 (eq S85) shows that in the Heisenberg picture, the action of the squeezing operation transforms the annihilation and creation operators, as follows

$$\begin{aligned}
\hat{a}' &= \hat{S}(r)^\dagger \hat{a} \hat{S}(r) = \cosh(r)\hat{a} + \sinh(r)\hat{a}^\dagger \\
(\hat{a}')^\dagger &= \hat{S}(r)^\dagger \hat{a}^\dagger \hat{S}(r) = \cosh(r)\hat{a}^\dagger + \sinh(r)\hat{a}
\end{aligned} \tag{22}$$

Substituting eq 22 into 3, we find that the single mode squeezed state is again Gaussian with the following covariance matrix (eq S92)

$$\sigma'(r) = \frac{1}{2}\begin{bmatrix} \cosh^2(r) + \sinh^2(r) & 2\cosh(r)\sinh(r) \\ 2\cosh(r)\sinh(r) & \cosh^2(r) + \sinh^2(r) \end{bmatrix} \tag{23}$$

Generalizing to $M > 1$ modes, we have

$$\sigma_{\mathrm{sque}} = \frac{1}{2}\begin{bmatrix} \bigoplus_{j=1}^M \cosh^2(r_j) + \sinh^2(r_j) & \bigoplus_{j=1}^M 2\cosh(r_j)\sinh(r_j) \\ \bigoplus_{j=1}^M 2\cosh(r_j)\sinh(r_j) & \bigoplus_{j=1}^M \cosh^2(r_j) + \sinh^2(r_j) \end{bmatrix}. \tag{24}$$

Next, we evaluate the effect of the M-mode interferometer on the squeezed state covariance matrix by starting from the simplest two-mode case and then obtaining the M-mode case.

The smallest interferometer is the two-mode beam splitter. It transforms a two-mode state according to the following operator

https://doi.org/10.1021/acs.jctc.4c00384
J. Chem. Theory Comput. 2024, 20, 6402−6413

$$\hat{B}(\theta) = e^{\theta(\hat{a}_1^\dagger \hat{a}_2 - \hat{a}_1 \hat{a}_2^\dagger)} \tag{25}$$

where $\theta \in [0, 2\pi]$ is a given angle. In the Heisenberg picture, $\hat{B}(\theta)$ transforms the annihilation operators, as follows

$$\hat{a}_1' = B(\theta)^\dagger \hat{a}_1 B(\theta) = \cos(\theta)\hat{a}_1 + \sin(\theta)\hat{a}_2$$
$$\hat{a}_2' = B(\theta)^\dagger \hat{a}_2 B(\theta) = \cos(\theta)\hat{a}_2 - \sin(\theta)\hat{a}_1 \tag{26}$$

Hence, for $k = 1$ and 2, we obtain

$$\hat{a}_k' = \sum_{j=1}^{2} U_{kj}\hat{a}_j$$
$$(\hat{a}_k')^\dagger = \sum_{j=1}^{2} U_{kj}^* \hat{a}_j^\dagger \tag{27}$$

where $U = U(\theta) = \begin{bmatrix} \cos(\theta) & \sin(\theta) \\ -\sin(\theta) & \cos(\theta) \end{bmatrix}$ is a unitary transformation. Additionally, when a phase-shifter is placed after the beam splitter such that $\hat{a}_1 \to e^{i\phi_1}\hat{a}_1$ for $\phi_1 \in [0, 2\pi]$, the resulting unitary transformation becomes

$$U = U(\theta, \phi_1) = \begin{bmatrix} \cos(\theta)e^{i\phi_1} & \sin(\theta)e^{i\phi_1} \\ -\sin(\theta) & \cos(\theta) \end{bmatrix}$$

Note that any 2×2 unitary matrix U can be implemented like this using a beam splitter and a phase-shifter with a suitable choice of values for θ and ϕ_1.[44] The generalization to M modes is straightforward and involves an M-mode interferometer, as follows

$$\hat{a}_k' = \sum_{j}^{M} U_{kj}\hat{a}_j$$
$$(\hat{a}_k')^\dagger = \sum_{j}^{M} U_{kj}^* \hat{a}_j^\dagger \tag{28}$$

where U is now an $M \times M$ unitary matrix. Substituting eq 28 into 3, we find that the M-mode interferometer U transforms an arbitrary covariance matrix $\tilde{\sigma}$, as follows (eq S95)

$$\sigma_{\text{rot}} = \begin{bmatrix} U & 0 \\ 0 & U^* \end{bmatrix} \tilde{\sigma} \begin{bmatrix} U^* & 0 \\ 0 & U \end{bmatrix}^T \tag{29}$$

Therefore, the outgoing Gaussian state obtained by rotating an M-mode squeezed vacuum state is described by the following covariance matrix

$$\sigma_{\text{out}} = \begin{bmatrix} U & 0 \\ 0 & U^* \end{bmatrix} \sigma_{\text{sque}} \begin{bmatrix} U^* & 0 \\ 0 & U \end{bmatrix}^T \tag{30}$$

With the general covariance matrix defined, we now explain how the parameters of the squeezers and interferometer are obtained to ensure that σ_{out} corresponds to eq 15, with kernel K defined by eq 13.

According to Takagi's matrix factorization, the symmetric matrix A can be decomposed, as followswhere Σ is the diagonal

$$A = U\Sigma U^T = U\left(\frac{1}{c}\bigoplus_{j=1}^{M} \tanh(r_j)\right)U^T, \tag{31}$$

matrix of singular values of A, and $0 < c < \lambda_1^{-1}$ is a rescaling parameter, with $\lambda_1 > 0$ the maximum eigenvalue of A. The rescaling ensures that every singular value can be represented as $\tanh(r_j)/c$ (note that $|\tanh(r)| < 1$ for all $r \in \mathbb{R}$). The unitary matrix U is used to parametrize the M-mode interferometer. The resulting covariance defined by eq 30 is consistent with the kernel K, introduced by eq 13, as shown in the Supporting Information 5 where eq 13 is obtained by substituting eqs 30 into 10.

Section 2.4 introduces an efficient implementation of the multimode Gaussian, with hardware efficiency, by first squeezing each mode and then implementing U in the MPS format by using an M-mode passive interferometer. Measurement of the modes generates a probability distribution of photon outcomes as defined by eq 17. We note that the theoretical analyses in this subsection neglects errors in the squeezed states, which could potentially hinder the performance of the quantum device.[45] More detailed investigation is the subject of follow up research studies of this initial theoretical proposal.

2.4. Holographic Implementation. Figures 3 and 4 illustrate the implementation of circuits corresponding to the state of a system of four modes, such as a multimode Gaussian state, in MPS format. Note that each beam splitter (BS) couples two adjacent bosonic modes.

2.4.1. MPS Circuits. Figure 3a shows the MPS circuit with one layer of beam splitters, inspired by a circuit previously proposed for moderately entangled quantum states.[29] Figure 3c shows a compact 3D cQED device that could implement the circuit with hardware efficiency using the so-called holographic quantum computing approach shown in Figure 3b. Note that the circuits shown in Figure 3a,b are equivalent. The only difference is that the circuit in (b) repurposes the modes after measurement. Mode 1 (q_1) is measured after squeezing and coupling with mode 2 by implementing the gates S_1, S_2, and BS_{12}. After that measurement, mode 1 can be repurposed for representing mode 3 (q_3) by first squeezing with S_3 and coupling it with mode 2 according to BS_{23}. Mode 2 is measured and then repurposed as mode 4. After applying S_4, BS_{34}, modes 3 and 4 are measured completing the implementation of the circuit with four modes using a two-mode quantum device. Circuits with more modes could be implemented analogously with the two-mode device by iterative squeezing, coupling, and measuring modes. Figure 3a,b also show that the gate cost of our holographic algorithm is $O(m)$ for an m-mode Gaussian state.

States with more entanglement can also be implemented with hardware efficiency by employing a few more modes. As an example, Figure 4a shows a four-mode circuit with a higher level of entanglement established by a second layer of beam splitters. Here, we implement the circuit by employing a three-mode device. Figure 4b shows the holographic implementation starting with gates S_1, S_2, S_3, BS_{12}, BS_{23}, and BS_{12}', which could be implemented with the device illustrated in Figure 4c. Mode 1 would be measured first and repurposed for representing mode 4. After this resetting, gates S_4, BS_{34}, BS_{23}', and BS_{34}' are implemented, and modes 2−4 are finally measured. The resulting sampling is equivalent to that of the conventional GBS experiment.

2.4.2. Parametrization. In this section, we explain how we parametrize the beam splitters employed in the MPS circuits introduced in Section 2.4.1, including the quantum circuits shown in Figures 3 and 4 with one and two layers of beam

https://doi.org/10.1021/acs.jctc.4c00384
J. Chem. Theory Comput. 2024, 20, 6402−6413

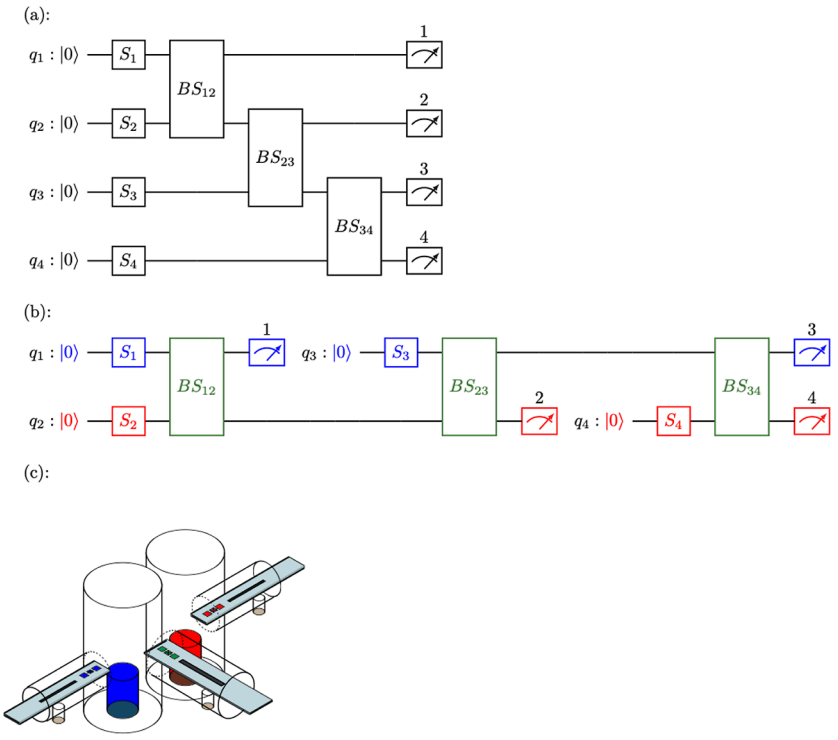

Figure 3. (a) Quantum circuit for a system with four modes, implemented by squeezing gates and one layer of beam splitters. (b) Holographic implementation of the circuit shown in panel (a) by repurposing two modes. The upper wire (blue) and lower wire (red) correspond to the two cavities of the same colors in (c), coupled by a transmon as a beam splitter (olive green). (c) 3D cQED device of two modes implemented with microwave cavity resonators coupled by a transmon.

splitters. As discussed in Section 4, the resulting parametrization allows for efficient and accurate GBS simulations based on arbitrary adjacency matrices.

First, we obtain the covariance matrix of the reference state σ_{ref} as well as the single-mode squeezing parameters from the adjacency matrix A, as described in Section 2.3.5. Next, we prepare the single-mode squeezed states from vacuum and feed them into the MPS-based network with variational beam-splitting and phase-shifting parameters $[\theta = (\theta_1, ..., \theta_K), \phi = (\phi_1, ..., \phi_K)]$ for a network with a total of K beam splitters. These parameters are optimized by minimization of the Frobenius distance $d_{\text{tmp}}(\theta, \phi) = \|\sigma_{\text{tmp}}(\theta, \phi) - \sigma_{\text{ref}}\|_F$ using a standard conjugate gradient-descent optimizer, which has the computational complexity of $O(dm^4)$ for an m-mode covariance matrix, where d is the number of iterations. The parameter set θ_{fin}, ϕ_{fin} corresponding to the minimal distance is then used as parameters for the quantum circuits.

2.5. Bosonic cQED Hardware Setup for Holographic GBS. The experimental requirements for implementing the holographic GBS include a high-coherence multimode cavity system (with at least two storage modes), pairwise beam-splitter operations with programmable phases and splitting ratios, and efficient readout, reset, and squeezing of individual cavity states. We emphasize that all of these requirements are already met simultaneously in existing hardware demonstrations, although design optimization is needed. For example, the two-mode device used to demonstrate bosonic two-qubit gates in ref 46, as reproduced in Figure 3c, can already be used to implement GBS of arbitrarily number of modes in principle using the circuits shown in Figure 3b. More recent demonstration of a quantum router connecting four storage modes[47] provides all the tools necessary to implement the holographic GBS routine with added beam-splitter layers such as those shown in Figure 4b. In this section, we briefly review the techniques necessary to physically implement the required bosonic operations, discuss the limitations of existing hardware, and introduce a minimal construction of the 3D circuit QED device tailored for holographic GBS.

Simply speaking, the key figure of merit that characterizes the performance of a device hardware for the proposed GBS protocol is the ratio of cavity coherence times to the operational cycle time. This ratio sets an upper bound on the executable circuit depth or effective number of modes that can be computed. The current state of the art in multimode cavity QED has led to quantum control of over 10 cavity modes with millisecond lifetimes.[48] The coaxial stub geometry, which is more widely adopted, consistently exhibits coherence times at the millisecond level. It also offers spatial separation of the modes, facilitating individual control.[46] In principle, seamless designs of superconducting cavities, leveraging low surface-to-volume ratio and materials-processing technologies borrowed from particle accelerators, can achieve coherence times on the order of seconds.[49] This represents a significant potential for enhancing system performance by several orders of magnitude.

Programmable two-mode beam splitter and single-mode squeezing gates can be achieved with either the four-wave mixing or the three-wave mixing process using external microwave pumps in 3D circuit QED. In either case, the external pump, applied under the appropriate frequency matching condition, can activate a rotating-frame Hamiltonian of the form $\hat{a}^\dagger \hat{b} e^{i\theta_i} + \hat{a}\hat{b}^\dagger e^{-i\theta_i}$ for photon conversion between $\hat{a}$ and $\hat{b}$ modes or $\hat{a}^{\dagger 2} e^{i\phi_i} + \hat{a}^2 e^{-i\phi_i}$ for squeezing drives in mode $\hat{a}$ for the ith beamsplitter. The phase of the pump tone controls

https://doi.org/10.1021/acs.jctc.4c00384
J. Chem. Theory Comput. 2024, 20, 6402−6413

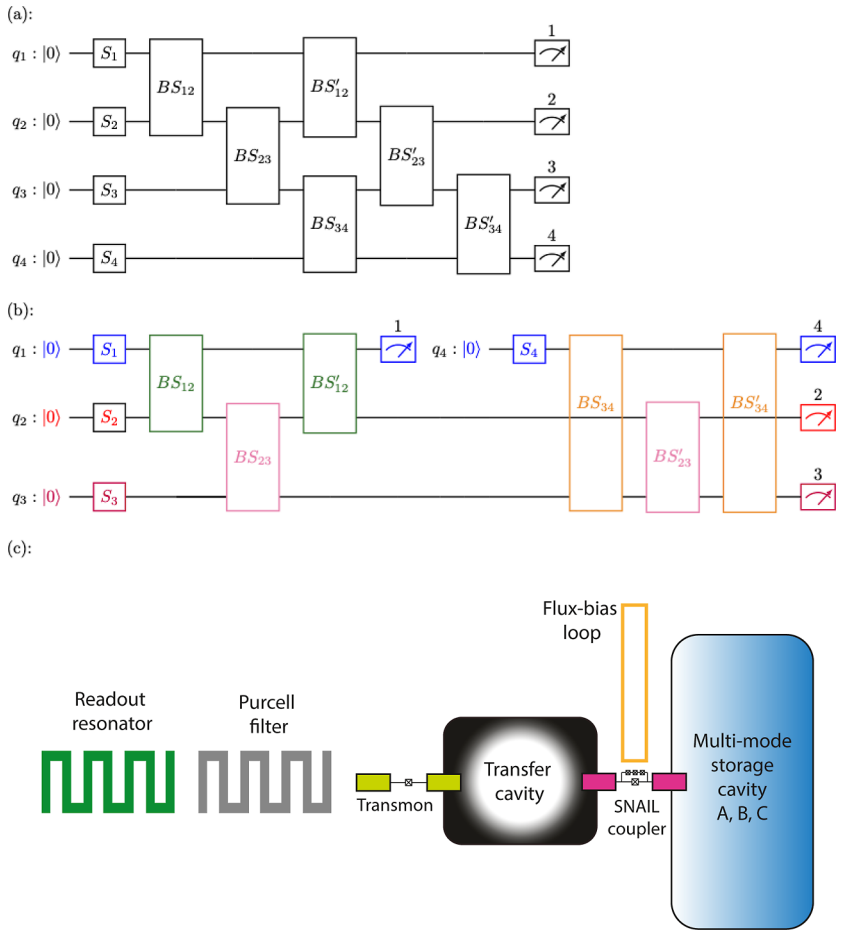

Figure 4. (a) Quantum circuit for a system with four modes, implemented by squeezing gates and two layers of beam splitters. (b) Holographic implementation of the circuit shown in panel (a) by repurposing three modes. Gates with the same color are simultaneously applied. (c) Multimode 3D cQED device implemented with microwave cavity resonators coupled by a transmon implemented as a quantum router.

the beam-splitting phase θ_i or the squeezing phase ϕ_i, while the amplitude and length of the external pump controls the splitting ratio or squeezing ratio. The four-wave mixing process is ubiquitously available in standard circuit QED hardware systems today, requiring only a fixed-frequency transmon ancilla, which generally allows for gates on the order of several μs.[50] Much faster gates on 100 ns scale or shorter can be implemented with parametric charge or flux drives[51,52] using novel Josephson ancilla circuitry that supports three-wave mixing processes. These ancillae, including, for example, SNAIL (Superconducting Nonlinear Asymmetric Inductive eLement),[47,53−55] RF SQUID, and ATS[56] have been under intensive development recently. Their integration with high-coherence 3D systems has led to record beam-splitter fidelity in the range of 99.9−99.99%.[51,52]

Measurement and reset of cavities can use transmons' ancillae and their low-Q readout resonators. A transmon qubit dispersively coupled to both a storage cavity and a readout resonator has been a well-developed tool to analyze the storage photon number using Ramsey sequences or selective transmon excitations.[57] If the task is to distinguish between $|0\rangle$ and $|1\rangle$ for the cavity, a Ramsey-like protocol for photon-number parity measurement is preferable for its faster speed, which should allow cavity measurements within 1 μs for typical coupling parameters. Cavity-state reset for arbitrary initial photon number can employ a beam splitter between the cavity and a linear low-Q mode (such as the readout resonators in Figure 3c). To achieve a reasonable operation speed (μs or less), however, requires a dedicated parametric coupler capable of strong three-wave mixing (e.g., a SNAIL). Assuming the expected number of cavity photons is low, an alternative approach involves resetting specific number states to vacuum through intermediary transmon states. Specifically, it is possible to convert a single-photon excitation in the storage cavity into double excitations in the transmon using a four-wave mixing drive. Subsequently, resetting the transmon should allow the resetting of the cavity $|1\rangle$ state within 1 μs.

In constructing a full device capable of the proposed holographic GBS, a key consideration is the ability to measure and reset one cavity mode without affecting the other cavity modes. Therefore, a transmon ancilla with simultaneous dispersive coupling to multiple storage modes for their readout, such as in ref 48, is undesirable. Instead of designing spatially separated storage cavity modes with independent transmon ancillas as in refs 47 and 50, we propose a hardware-efficient setup that satisfies all the requirements as in Figure 4c. The storage cavity module containing multiple modes is coupled to a three-wave mixing coupler (e.g., SNAIL) operated under the condition to minimize the fourth-order nonlinearity of the storage modes (self Kerr and cross Kerr). The three-wave coupler is further coupled to another high-Q transfer cavity with a transmon ancilla. The three-wave coupler allows for fast beam-splitter operations between storage modes as well as swapping between any storage mode and the transfer cavity

https://doi.org/10.1021/acs.jctc.4c00384
J. Chem. Theory Comput. 2024, 20, 6402−6413

(typically prepared in vacuum) for readout and initialization. The number of photons in the transfer cavity can be analyzed by leveraging the dispersive interaction with the transmon. Additionally, the reset of the transfer cavity can be carried out using transmon-mediated sideband drives, which are conditioned on the cavity states. Utilizing the transfer cavity not only protects the storage modes from spurious fourth-order nonlinearities but also protects the low-Q components of the circuits, which are required for fast measurement and reset.

3. RESULTS AND DISCUSSION

We first demonstrate the capabilities of the MPS-based holographic approach as applied to GBS for solving the problem of molecular docking (Section 3.1). Next, we analyze the scalability of the approach as applied to random adjacency matrices (Section 3.2).

3.1. Molecular Docking Mapped as a Graph Search Problem. In this section, we apply the MPS-based holographic approach to solve the molecular docking problem, which involves finding the optimal binding mode of a small drug molecule bound to a target biological receptor. Specifically, we focus on the benchmark model system of a thiol-containing AS compound bound to the TACE, shown in Figure 2, that allows for direct comparisons of our MPS-based GBS approach to full GBS simulations.[21] Binding of AS to TACE is determined by hydrogen bonds and hydrophobic contacts established by six pharmacophores in the TACE active site and four pharmacophores in the AS. Therefore, there is a total of 24 possible pairs of interactions that could be established upon AS binding.

The binding interaction graph is thus defined by a 24 × 24 adjacency matrix A, where $A_{ij} = A_{ji}$ is nonzero if the two binding interactions i and j are geometrically compatible and $A_{ij} = 0$ otherwise. With this adjacency matrix, the GBS routine is carried out as described in Section 2.1, and the corresponding MPS-based holographic implementation is carried out as described in Section 2.4. The results of the sampling are analyzed to identify the densest sampled subgraph.

Figure 5 shows the result of GBS versus MPS-network sampling. Dense subgraphs sampled by GBS are converted into heaviest cliques representing the most probable binding patterns using the algorithm for postprocessing GBS data described in ref 21. The algorithm first shrinks the GBS sampled subgraph into smaller cliques by sequentially removing vertices with small degree until finding a clique. Then, the found clique is locally expanded into a large clique according to a local search algorithm that expands the clique by one vertex that is fully connected with all vertices in the original clique. As shown in Figure 5a, the sampling routines successfully identify the heaviest clique (weight = 3.99) with high probability. Moreover, sampling results from the MPS network agree closely with the GBS result, confirming the accuracy of the proposed MPS-based holographic approach. Figure 5b plots the maximum clique as a subgraph in the binding interaction graph, while Figure 5c visualizes the binding interactions that correspond to the maximum clique.

3.2. Scalability Analysis with Random Graphs. Here, we examine the scalability and accuracy of the MPS-based algorithm described in Section 2.4 for a series of random graphs specified by randomly generated adjacency matrices A that satisfy the conditions described at the beginning of Section 2.1.

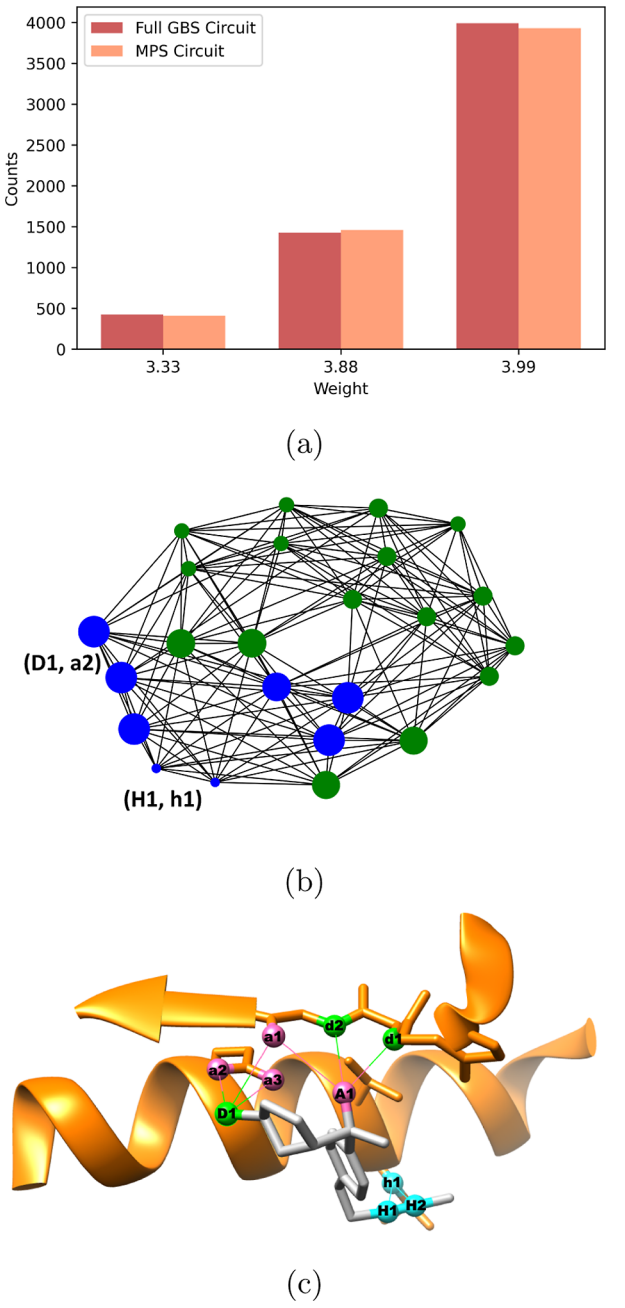

Figure 5. (a) Weight of sampled clique from both MPS-based network and full GBS network after postselection. Only three weights (3.33, 3.88, and 3.99) are selected with high frequency. (b) Subgraph for the heaviest (weight = 3.99) clique obtained in (a). (c) Visualization of binding interactions of the subgraph in (b).

First, we examine the capabilities of our variational approach to approximate the full optical network by comparing the covariance matrix at the output of the optimized MPS-based holographic network to the reference covariance matrix generated by the conventional GBS setup (Table 1).

The results displayed in Table 1 indicate that MPS-circuits equipped with either one or two layers of beam splitters achieve high precision in approximating the GBS output states, showing that the covariance matrix error remains below 5%, even for circuits comprising up to 50 modes.

https://doi.org/10.1021/acs.jctc.4c00384
J. Chem. Theory Comput. 2024, 20, 6402−6413

Table 1. Performance of the MPS-Based Circuits Parameterized by the Variational Covariance Matrix Optimization[a]

M	distance
(a) 1-layer MPS network	
12	0.05
16	0.04
20	0.04
24	0.03
50	0.02
(b) 2-layer MPS network	
12	0.04
16	0.04
20	0.03
24	0.02
50	0.01

[a]The number of modes for each test is denoted by M. The relative distance between covariance matrices is defined as $\|\sigma_{opt} - \sigma_{ref}\|/\|\sigma_{ref}\|$.

4. CONCLUSIONS

In this study, we have introduced quantum circuits designed for simulating multimode state vectors on 3D cQED processors, leveraging MPS representations. These circuits have been showcased through simulations of molecular docking, specifically focusing on the binding of a thiol-containing AS ligand to the tumor necrosis factor-α converting enzyme receptor, utilizing holographic GBS. Our findings reveal the proposed MPS scheme based on cQED devices with only 2 or 3 modes is able to prepare multimode Gaussian states that closely approximate those obtained by the conventional GBS method even for systems with up to 50 modes. This approach opens the door to a broad spectrum of GBS applications that could be efficiently executed on compact 3D cQED processors using the holographic method.

■ ASSOCIATED CONTENT

Data Availability Statement

The python code for the TACE−AS GBS/MPS simulation is available at https://colab.research.google.com/drive/1_cWqkU42e5jCtnwwFfd833eBaYsqhLV6?usp=sharing

Supporting Information

The Supporting Information is available free of charge at https://pubs.acs.org/doi/10.1021/acs.jctc.4c00384.

Derivations for the P-representation, Husimi representation, sampled probabilities of multimode Gaussian states, and covariance matrices of squeezed and rotated multimode Gaussian states (PDF)

■ AUTHOR INFORMATION

Corresponding Author

Victor S. Batista − *Department of Chemistry, Yale University, New Haven, Connecticut 06520, United States; Yale Quantum Institute, Yale University, New Haven, Connecticut 06511, United States;* orcid.org/0000-0002-3262-1237; Email: victor.batista@yale.edu

Authors

Ningyi Lyu − *Department of Chemistry, Yale University, New Haven, Connecticut 06520, United States;* orcid.org/0000-0001-9239-9925

Paul Bergold − *Department of Mathematics, University of Surrey, Guildford GU2 7XH, U.K.;* orcid.org/0000-0003-3033-0732

Micheline B. Soley − *Department of Chemistry, Yale University, New Haven, Connecticut 06520, United States; Yale Quantum Institute, Yale University, New Haven, Connecticut 06511, United States; Department of Chemistry, University of Wisconsin−Madison, Madison, Wisconsin 53706, United States;* orcid.org/0000-0001-7973-2842

Chen Wang − *Department of Physics, University of Massachusetts-Amherst, Amherst, Massachusetts 01003, United States*

Complete contact information is available at: https://pubs.acs.org/10.1021/acs.jctc.4c00384

Notes

The authors declare no competing financial interest.

■ ACKNOWLEDGMENTS

The authors acknowledge support from the NSF grant 2124511 [CCI Phase I: NSF Center for Quantum Dynamics on Modular Quantum Devices (CQD-MQD)].

■ REFERENCES

(1) McDermott, M. J.; Dwaraknath, S. S.; Persson, K. A. A graph-based network for predicting chemical reaction pathways in solid-state materials synthesis. *Nat. Commun.* **2021**, *12*, 3097.

(2) Hashemi, A.; Bougueroua, S.; Gaigeot, M.-P.; Pidko, E. A. ReNeGate: A Reaction Network Graph-Theoretical Tool for Automated Mechanistic Studies in Computational Homogeneous Catalysis. *J. Chem. Theory Comput.* **2022**, *18*, 7470−7482.

(3) Ratkiewicz, A.; Truong, T. N. Application of Chemical Graph Theory for Automated Mechanism Generation. *J. Chem. Inf. Comput. Sci.* **2003**, *43*, 36−44.

(4) García-Domenech, R.; Gálvez, J.; de Julián-Ortiz, J. V.; Pogliani, L. Some New Trends in Chemical Graph Theory. *Chem. Rev.* **2008**, *108*, 1127−1169.

(5) Burch, K. J. *Chemical Applications of Graph Theory*; Elsevier, 2019; pp 261−294.

(6) Aldeghi, M.; Coley, C. W. A graph representation of molecular ensembles for polymer property prediction. *Chem. Sci.* **2022**, *13*, 10486−10498.

(7) Gutman, I.; Ruscić, B.; Trinajstić, N.; Wilcox, C. F. Graph theory and molecular orbitals. XII. Acyclic polyenes. *J. Chem. Phys.* **1975**, *62*, 3399−3405.

(8) Gutman, I.; Polansky, O. E. *Chapter 5 Graph Theory and Molecular Orbitals*; De Gruyter, 1986; pp 42−45.

(9) Mohapatra, S.; An, J.; Gómez-Bombarelli, R. Chemistry-informed macromolecule graph representation for similarity computation, unsupervised and supervised learning. *Mach. Learn.: Sci. Techno.* **2022**, *3*, 015028.

(10) Valiant, L. The complexity of computing the permanent. *Theor. Comput. Sci.* **1979**, *8*, 189−201.

(11) Bezáková, I.; Štefankovič, D.; Vazirani, V. V.; Vigoda, E. Accelerating Simulated Annealing for the Permanent and Combinatorial Counting Problems. *SIAM J. Comput.* **2008**, *37*, 1429−1454.

(12) Aaronson, S.; Arkhipov, A. The computational complexity of linear optics. In *Proceedings of the Forty-Third Annual ACM Symposium on Theory of Computing*, 2011; pp 333−342.

(13) Troyansky, L.; Tishby, N. On the quantum evaluation of the determinant and the permanent of a matrix. *Proc. Phys. Comput.* **1996**, *96*, 1.

(14) Motes, K. R.; Gilchrist, A.; Dowling, J. P.; Rohde, P. P. Scalable boson sampling with time-bin encoding using a loop-based architecture. *Phys. Rev. Lett.* **2014**, *113*, 120501.

(15) Thekkadath, G.; Sempere-Llagostera, S.; Bell, B.; Patel, R.; Kim, M.; Walmsley, I. Experimental Demonstration of Gaussian Boson Sampling with Displacement. *PRX Quantum* **2022**, *3*, 020336.
(16) Spagnolo, N.; Brod, D. J.; Galvão, E. F.; Sciarrino, F. Non-linear Boson Sampling. *npj Quantum Inf.* **2023**, *9*, 3.
(17) Wang, H.; He, Y.; Li, Y. H.; Su, Z. E.; Li, B.; Huang, H. L.; Ding, X.; Chen, M. C.; Liu, C.; Qin, J.; et al. High-efficiency multiphoton boson sampling. *Nat. Photonics* **2017**, *11*, 361−365.
(18) Wang, C. S.; Curtis, J. C.; Lester, B. J.; Zhang, Y.; Gao, Y. Y.; Freeze, J.; Batista, V. S.; Vaccaro, P. H.; Chuang, I. L.; Frunzio, L.; Jiang, L.; Girvin, S.; Schoelkopf, R. J. Efficient Multiphoton Sampling of Molecular Vibronic Spectra on a Superconducting Bosonic Processor. *Phys. Rev. X* **2020**, *10*, 021060.
(19) Huh, J.; Guerreschi, G. G.; Peropadre, B.; McClean, J. R.; Aspuru-Guzik, A. Boson sampling for molecular vibronic spectra. *Nat. Photonics* **2015**, *9*, 615−620.
(20) Peropadre, B.; Guerreschi, G. G.; Huh, J.; Aspuru-Guzik, A. Proposal for Microwave Boson Sampling. *Phys. Rev. Lett.* **2016**, *117*, 140505.
(21) Banchi, L.; Fingerhuth, M.; Babej, T.; Ing, C.; Arrazola, J. M. Molecular docking with Gaussian Boson Sampling. *Sci. Adv.* **2020**, *6*, No. eaax1950.
(22) Quesada, N.; Chadwick, R. S.; Bell, B. A.; Arrazola, J. M.; Vincent, T.; Qi, H.; García-Patrón, R. Quadratic Speed-Up for Simulating Gaussian Boson Sampling. *PRX Quantum* **2022**, *3*, 010306.
(23) Blais, A.; Grimsmo, A. L.; Girvin, S. M.; Wallraff, A. Circuit quantum electrodynamics. *Rev. Mod. Phys.* **2021**, *93*, 025005.
(24) Hamilton, C. S.; Kruse, R.; Sansoni, L.; Barkhofen, S.; Silberhorn, C.; Jex, I. Gaussian boson sampling. *Phys. Rev. Lett.* **2017**, *119*, 170501.
(25) Brádler, K.; Dallaire-Demers, P. L.; Rebentrost, P.; Su, D.; Weedbrook, C. Gaussian boson sampling for perfect matchings of arbitrary graphs. *Phys. Rev. A* **2018**, *98*, 032310.
(26) Oh, C.; Fefferman, B.; Jiang, L.; Quesada, N. Quantum-Inspired Classical Algorithm for Graph Problems by Gaussian Boson Sampling. *PRX Quantum* **2024**, *5*, 020341.
(27) He, Y.; Ding, X.; Su, Z.-E.; Huang, H.-L.; Qin, J.; Wang, C.; Unsleber, S.; Chen, C.; Wang, H.; He, Y.-M.; et al. Time-bin-encoded boson sampling with a single-photon device. *Phys. Rev. Lett.* **2017**, *118*, 190501.
(28) Foss-Feig, M.; Hayes, D.; Dreiling, J. M.; Figgatt, C.; Gaebler, J. P.; Moses, S. A.; Pino, J. M.; Potter, A. C. Holographic quantum algorithms for simulating correlated spin systems. *Phys. Rev. Res.* **2021**, *3*, 033002.
(29) Schön, C.; Solano, E.; Verstraete, F.; Cirac, J. I.; Wolf, M. M. Sequential generation of entangled multiqubit states. *Phys. Rev. Lett.* **2005**, *95*, 110503.
(30) Ran, S.-J. Encoding of matrix product states into quantum circuits of one-and two-qubit gates. *Phys. Rev. A* **2020**, *101*, 032310.
(31) Oseledets, I. V. Tensor-Train Decomposition. *SIAM J. Sci. Comput.* **2011**, *33*, 2295−2317.
(32) Lyu, N.; Soley, M. B.; Batista, V. S. Tensor-train split-operator KSL (TT-SOKSL) method for quantum dynamics simulations. *J. Chem. Theory Comput.* **2022**, *18*, 3327−3346.
(33) Lyu, N.; Mulvihill, E.; Soley, M. B.; Geva, E.; Batista, V. S. Tensor-train thermo-field memory kernels for generalized quantum master equations. *J. Chem. Theory Comput.* **2023**, *19*, 1111−1129.
(34) Brádler, K.; Friedland, S.; Izaac, J.; Killoran, N.; Su, D. Graph isomorphism and Gaussian boson sampling. *Spec. Matrices* **2021**, *9*, 166−196.
(35) Dias, R.; de Azevedo Jr, W.; Walter, F. Molecular docking algorithms. *Curr. Drug Targets* **2008**, *9*, 1040−1047.
(36) Kuhl, F. S.; Crippen, G. M.; Friesen, D. K. A combinatorial algorithm for calculating ligand binding. *J. Comput. Chem.* **1984**, *5*, 24−34.
(37) Miller, M. D.; Kearsley, S. K.; Underwood, D. J.; Sheridan, R. P. FLOG: a system to select 'quasi-flexible' ligands complementary to a receptor of known three-dimensional structure. *J. Comput. Aided Mol. Des.* **1994**, *8*, 153−174.
(38) Ewing, T. J.; Kuntz, I. D. Critical evaluation of search algorithms for automated molecular docking and database screening. *J. Comput. Chem.* **1997**, *18*, 1175−1189.
(39) Miller, M. D.; Sheridan, R. P.; Kearsley, S. K. SQ: a program for rapidly producing pharmacophorically relevant molecular superpositions. *J. Med. Chem.* **1999**, *42*, 1505−1514.
(40) Yang, S.-Y. Pharmacophore modeling and applications in drug discovery: challenges and recent advances. *Drug Discov. Today* **2010**, *15*, 444−450.
(41) Kitchen, D. B.; Decornez, H.; Furr, J. R.; Bajorath, J. Docking and scoring in virtual screening for drug discovery: methods and applications. *Nat. Rev. Drug Discovery* **2004**, *3*, 935−949.
(42) Poole, A. M.; Ranganathan, R. Knowledge-based potentials in protein design. *Curr. Opin. Struct. Biol.* **2006**, *16*, 508−513.
(43) Gohlke, H.; Klebe, G. Statistical potentials and scoring functions applied to protein−ligand binding. *Curr. Opin. Struct. Biol.* **2001**, *11*, 231−235.
(44) Reck, M.; Zeilinger, A.; Bernstein, H. J.; Bertani, P. Experimental realization of any discrete unitary operator. *Phys. Rev. Lett.* **1994**, *73*, 58−61.
(45) Drummond, P. D.; Opanchuk, B.; Dellios, A.; Reid, M. D. Simulating complex networks in phase space: Gaussian boson sampling. *Phys. Rev. A* **2022**, *105*, 012427.
(46) Gao, Y. Y.; Lester, B. J.; Chou, K. S.; Frunzio, L.; Devoret, M. H.; Jiang, L.; Girvin, S. M.; Schoelkopf, R. J. Entanglement of bosonic modes through an engineered exchange interaction. *Nature* **2019**, *566*, 509−512.
(47) Zhou, C.; Lu, P.; Praquin, M.; Chien, T.-C.; Kaufman, R.; Cao, X.; Xia, M.; Mong, R. S.; Pfaff, W.; Pekker, D.; et al. Realizing all-to-all couplings among detachable quantum modules using a microwave quantum state router. *npj Quantum Inf.* **2023**, *9*, 54.
(48) Chakram, S.; Oriani, A. E.; Naik, R. K.; Dixit, A. V.; He, K.; Agrawal, A.; Kwon, H.; Schuster, D. I. Seamless High-Q Microwave Cavities for Multimode Circuit Quantum Electrodynamics. *Phys. Rev. Lett.* **2021**, *127*, 107701.
(49) Romanenko, A.; Pilipenko, R.; Zorzetti, S.; Frolov, D.; Awida, M.; Belomestnykh, S.; Posen, S.; Grassellino, A. Three-Dimensional Superconducting Resonators at $T < 20$ mK with Photon Lifetimes up to $\tau = 2$ s. *Phys. Rev. Appl.* **2020**, *13*, 034032.
(50) Gao, Y. Y.; Lester, B. J.; Zhang, Y.; Wang, C.; Rosenblum, S.; Frunzio, L.; Jiang, L.; Girvin, S. M.; Schoelkopf, R. J. Programmable Interference between Two Microwave Quantum Memories. *Phys. Rev. X* **2018**, *8*, 021073.
(51) Chapman, B. J.; de Graaf, S. J.; Xue, S. H.; Zhang, Y.; Teoh, J.; Curtis, J. C.; Tsunoda, T.; Eickbusch, A.; Read, A. P.; Koottandavida, A.; Mundhada, S. O.; Frunzio, L.; Devoret, M.; Girvin, S.; Schoelkopf, R. High-On-Off-Ratio Beam-Splitter Interaction for Gates on Bosonically Encoded Qubits. *PRX Quantum* **2023**, *4*, 020355.
(52) Lu, Y.; Maiti, A.; Garmon, J. W. O.; Ganjam, S.; Zhang, Y.; Claes, J.; Frunzio, L.; Girvin, S. M.; Schoelkopf, R. J. A high-fidelity microwave beamsplitter with a parity-protected converter. **2023**, arXiv:2303.00959 [quant-ph].
(53) Frattini, N. E.; Vool, U.; Shankar, S.; Narla, A.; Sliwa, K. M.; Devoret, M. H. 3-wave mixing Josephson dipole element. *Appl. Phys. Lett.* **2017**, *110*, 222603.
(54) Hillmann, T.; Quijandría, F.; Johansson, G.; Ferraro, A.; Gasparinetti, S.; Ferrini, G. Universal Gate Set for Continuous-Variable Quantum Computation with Microwave Circuits. *Phys. Rev. Lett.* **2020**, *125*, 160501.
(55) Eriksson, A. M.; Sépulcre, T.; Kervinen, M.; Hillmann, T.; Kudra, M.; Dupouy, S.; Lu, Y.; Khanahmadi, M.; Yang, J.; Castillo-Moreno, C.; et al. Universal control of a bosonic mode via drive-activated native cubic interactions. *Nat. Commun.* **2024**, *15*, 2512.
(56) Lescanne, R.; Villiers, M.; Peronnin, T.; Sarlette, A.; Delbecq, M.; Huard, B.; Kontos, T.; Mirrahimi, M.; Leghtas, Z. Exponential suppression of bit-flips in a qubit encoded in an oscillator. *Nat. Phys.* **2020**, *16*, 509−513.
(57) Vlastakis, B.; Kirchmair, G.; Leghtas, Z.; Nigg, S. E.; Frunzio, L.; Girvin, S. M.; Mirrahimi, M.; Devoret, M. H.; Schoelkopf, R. J.

https://doi.org/10.1021/acs.jctc.4c00384
J. Chem. Theory Comput. 2024, 20, 6402−6413

Deterministically Encoding Quantum Information Using 100-Photon Schrödinger Cat States. *Science* **2013**, *342*, 607−610.

https://doi.org/10.1021/acs.jctc.4c00384
J. Chem. Theory Comput. 2024, 20, 6402−6413